Study of Junction and Tip Vortices Using Particle Displacement Velocimetry

A. Shekarriz,* T. C. Fu,† and J. Katz‡
Johns Hopkins University, Baltimore, Maryland 21218
and
H. L. Liu§ and T. T. Huang§
David Taylor Research Center, Bethesda, Maryland 20084

This paper describes experiments focusing on development of junction and tip vortices trailing behind a sail attached to an axisymmetric underwater body. These experiments were performed in a towing tank and involved implementation of particle displacement velocimetry. A map of the velocity at several streamwise locations was obtained, and the circulation was computed with 12–18% accuracy. The results reveal a reduction in the circulation of the junction vortex with increasing distance from the sail. This reduction seems to be more severe within the after-body than in the parallel middle-body section. The instantaneous circulation of the tip vortex remained fairly constant over the measured distance. Also, the distribution of circulation within the tip vortex core seems to follow a $\Gamma \propto r^2$ profile in the inner section and $\Gamma \propto \log r$ within the outer region. The strength of the tip vortex was nearly 12 times greater than the circulation of the junction vortex. The circulation of a typical wake vortex at zero incidence is comparable in strength to the junction vortex.

Introduction

TWO typical vortical structures that trail behind a wing attachment to the hull of a submarine or an aircraft fuselage are junction and tip vortices. The junction vortex causes an increase in wall shear stress, interacts with the surrounding boundary layer, and generates undesirable noise. Examples of the effects of a tip vortex are wing tip cavitation, limitation in airport capacity, and adverse effects of trailing vortices of one blade on the following blades in propulsors.

A junction vortex is produced whenever a boundary layer is protruded by an obstacle. As a result of the adverse pressure gradient upstream of the obstacle, the boundary layer separates from the surface and a system of lateral vortices is formed. Most of the studies on these vortices report a time-averaged velocity at the line of symmetry upstream of an ideal wing-body junction.[1] Beyond the axis of symmetry, the initial lateral vorticity is skewed and gradually converted into a horseshoe vortex.[2,3] When the boundary layer is laminar, the horseshoe vortex is reported to be steady and predictable.[4] As the Reynolds number (based on diameter of the obstacle) and the ratio of diameter to displacement thickness increase, the horseshoe vortex initially exhibits a periodic behavior and then becomes irregular.[5,6] Devenport and Simpson reported bimodal velocity histograms that they referred to as the two preferred modes (zero- and backflow modes) of the turbulent vortex.[7] These vortices have been shown to meander as they move downstream. Although there has been some work directed toward understanding the development of a longitudinal vortex pair embedded within a boundary layer,[8,9] the development of a horseshoe vortex along a body of revolution has not been directly investigated. As the present study shows, simulating the horseshoe vortex behind an appendage as a longitudinal vortex pair ignores the wake of the wing.

A tip vortex is formed as a result of the lift on a finite span wing.[10] The roll-up of a tip vortex starts around the tip[11] and continues far downstream of the wing.[12,13] El-Ramly and Rainbird[13] showed that, at 13 spans downstream of the wing, the roll-up process was not yet complete and 20% of the "root circulation" was still within the unrolled-up portion of the viscous wake.

The focus of this paper is the examination of the development of these two vortical structures. Because of the complexity and unsteady nature of the flow, resolving these vortical structures requires mapping the instantaneous velocity field. Consequently, the particle displacement velocimetry (PDV) method is opted for.

PDV consists of measuring the velocity of a tracer particle from its displacement during a short time interval. By including enough of these particles, one can make simultaneous multipoint measurements. A comprehensive review of particle displacement/image velocimetry may be found in Adrian[14] and Gharib and Willert.[15] Briefly, this technique involves illuminating a seeded section of a flowfield with a laser light sheet and recording a double-pulsed image of the tracer particles on a photographic film. Each moving particle leaves two traces on the film. The velocity of the particle is proportional to the distance between its corresponding two traces.

There are different methods of determining the distance between two consecutive traces. The particle tracking method involves matching traces of the *same* particle. Flow direction is identified by making the second trace longer. More details will be covered later and may also be found in Fu et al.[16] Another technique, the autocorrelation method, relies on computing the statistical average of displacement of all particles within a small window.[17] This process is then repeated throughout the entire field. In the former method, traces of individual particles must be isolated and distinguishable; the latter method, however, becomes more accurate as the analysis window includes a higher density of particle traces, some of which may overlap. A third technique, usually referred to as the particle speckle method, involves computing the Fourier transform of the particle shift optically.[14] Particle tracking has been utilized during the present study. The primary reason

---

Received Nov. 27, 1990; presented as Paper 91-0269 at the AIAA 29th Aerospace Sciences Meeting, Reno, NV, Jan. 7–10, 1991; revision received May 27, 1991; accepted for publication June 10, 1991.

*Postdoctoral Fellow, Department of Mechanical Engineering.

†Graduate Student.

‡Associate Professor. Member AIAA.

§Naval Architect, Ship Hydromechanics Department, Code 1542.

is our desire to examine the flow qualitatively while studying the junction vortex. Since this structure is embedded within a boundary layer, initial observations required some subjective judgments. The other two methods cannot be used for qualitative observations. Furthermore, because of the violent behavior of the junction vortex within the boundary layer, finding several neighboring particles with the same velocity is unlikely, even in windows as small as 0.5 mm^2. Thus correlation methods would fail to work within such an environment.[17]

The model used was an axisymmetric underwater body with an attached sail. The junction flow was studied at zero incidence, and the tip vortex was studied for a side slip angle of 5 deg. Both studies were performed at a Reynolds number of 7.2×10^4 (based on sail chord length) and 9×10^5 (based on the body length).

Visualization Setup and Procedure

Figure 1 is a schematic illustration of the experimental setup. This facility is located at the David Taylor Research Center. The dimensions of the towing tank used are $43 \times 3 \times 1.5$ m. The carriage was powered by two 7.5-kW dc motors capable of reaching a designed speed of 3.2 m/s. A feedback control system regulated the carriage velocity to within 0.1%. The carriage was designed to minimize vibrations and handle the required hydrodynamic loads associated with large models.

The model used was a submarine-like body, 30.5 cm in diameter and 2.72 m long. The sail was 5.3 cm in maximum thickness and 23.2 cm in chordlength, with a span of 12.7 cm, and was mounted on the model 57.6 cm from the leading edge. For the tip vortex experiments, a slightly different sail, usually referred to as the DARPA sail,[18] was used. This sail was 4 cm in thickness and 22 cm in chordlength, with a span of 12.7 cm. The model was mounted on a 5.1-cm-diameter stainless steel sting. The sting was fastened to a strut assembly that was attached to the carriage.

As shown in Fig. 1, the light source is a 6-W cw argon-ion laser. The laser beam was guided into an acousto-optic beam deflector (Bragg cell), a set of spherical lenses, an iris diaphragm, and a cylindrical lens for expanding the beam into a sheet. A sheet thickness of 6.3 cm was iteratively shown to work best for these experiments. An electronic control system enabled generation of any desired combination of laser pulses. The duration of pulses and the delay between the two pulses were selected based on several parameters. These parameters were particle residence time within the sheet (the ratio of the sheet thickness to the velocity normal to the sheet), the aspect ratio of the long trace, and the delay between the two traces (Fig. 3). The latter were dictated by the velocity components within the sheet.

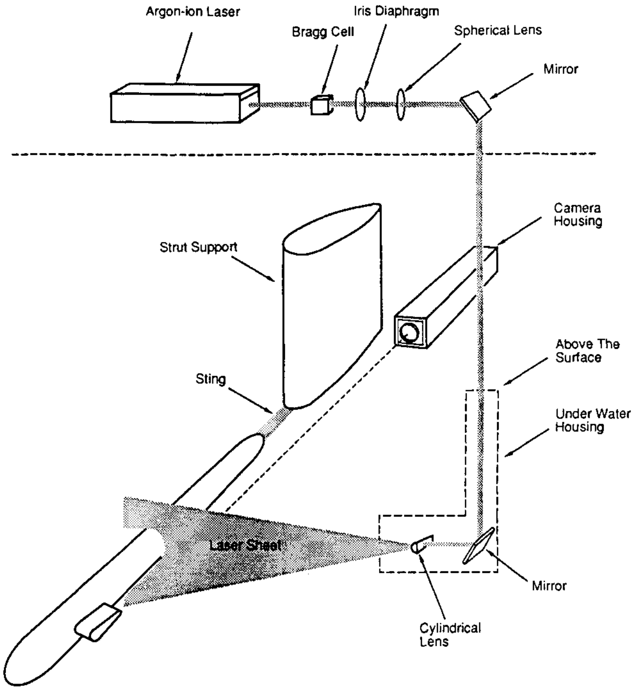

Fig. 1 Schematic diagram of the experimental setup.

The residence time is a variable and cannot be determined without any prior knowledge about the flowfield. Based on several trials, the respective average duration of the first pulse, delay between exposures, and duration of the second pulse were 5, 25, and 25 ms and 3, 15, and 15 ms for the junction and tip vortex studies, respectively (the second pulse was made longer for identifying the flow direction). Long exposures increased the chance of obtaining incomplete illumination codes, particularly in regions of high longitudinal velocity, but increased the accuracy in regions of low velocity. Thus, a short exposure created a bias against low lateral velocities and, conversely, a long exposure caused a bias against high lateral velocities.

Particles containing embedded fluorescent dye were used for the present study. They were manufactured at Johns Hopkins University by using a process developed specifically to generate large quantities at a reasonable cost. Their size ranged between 10 and 50 μm in diameter with a mean of 26 μm and a standard deviation of 8 μm. The specific gravity of these particles ranged between 0.94 and 1.06. Freestream seeding upstream of the model was adopted because, unlike surface injection, it did not interfere with the boundary layer.

Recording Setup and Procedure

The images were recorded by a 35-mm still camera with a remotely controlled motor assembly to focus and zoom the lens. A small CCD video camera was placed behind the viewfinder of the 35-mm camera for the purpose of focusing. Typically, the focal length was kept in the 200–400-mm range, whereas the aperture was varied between f/2.8 and f/5.6. This setup enabled focusing on areas ranging from 10.2×15.2 cm to 15.2×22.9 cm. The images were recorded on 3200ASA Kodak-TMAX film with a resolution of 125 line pairs/mm. The camera assembly was placed inside a sealed Plexiglas® housing with a polished glass front window. The camera housing was placed at the bottom of the tank on a lockable platform to ensure a repeatable position and angle of observation. The frame of reference and magnification were established by recording images of a reference scale prior to each run.

A specially designed electronic control unit was responsible for controlling the camera shutter and synchronizing with the laser pulses. An "electronic eye" was used for detecting the location of the model and initiating the recording process. During each run, several images were recorded at axial intervals of 22.5 cm ($\Delta x/c = 0.98$). The above procedure was repeated again after waiting sufficiently long for the secondary flow in the tank to settle. This relaxation time was usually 30 min or more.

Figure 2a is a schematic diagram of the interrogation regions for studying the tip and junction vortices. Figure 2b is a typical picture of a junction vortex and its surrounding flow downstream of the sail, and Fig. 2c is a sample image of the tip vortex with the body at a side slip angle of 5 deg. In the photographs, the shorter exposure precedes the longer one. The intersection of the laser sheet with the body is shown as a bright arc.

Image Processing and Analysis

After being developed, each negative was illuminated from behind with a diffuse light and examined by a 700-line video camera. This camera was mounted on a precision stage and equipped with a microscope objective that focused on an area of 3×3 mm^2. Each video frame was digitized to a 512×480-pixel array. An ITEX 100 image processor board, inserted

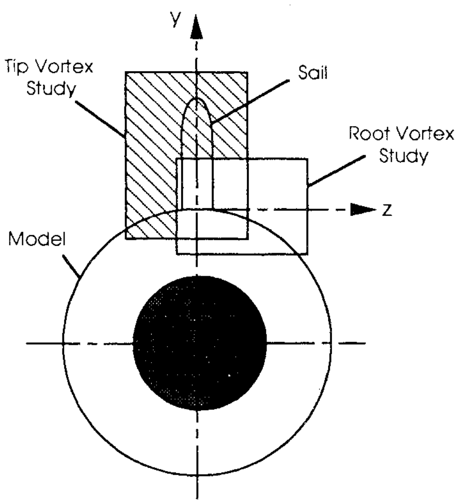

Fig. 2a Schematics of the interrogation area, rear view.

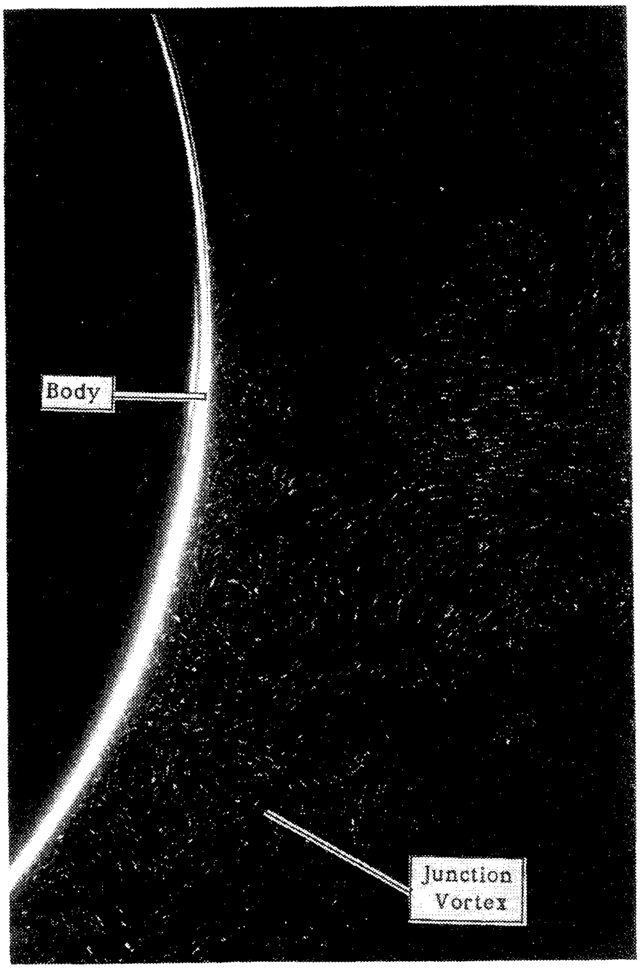

Fig. 2b A typical photograph of the junction vortex.

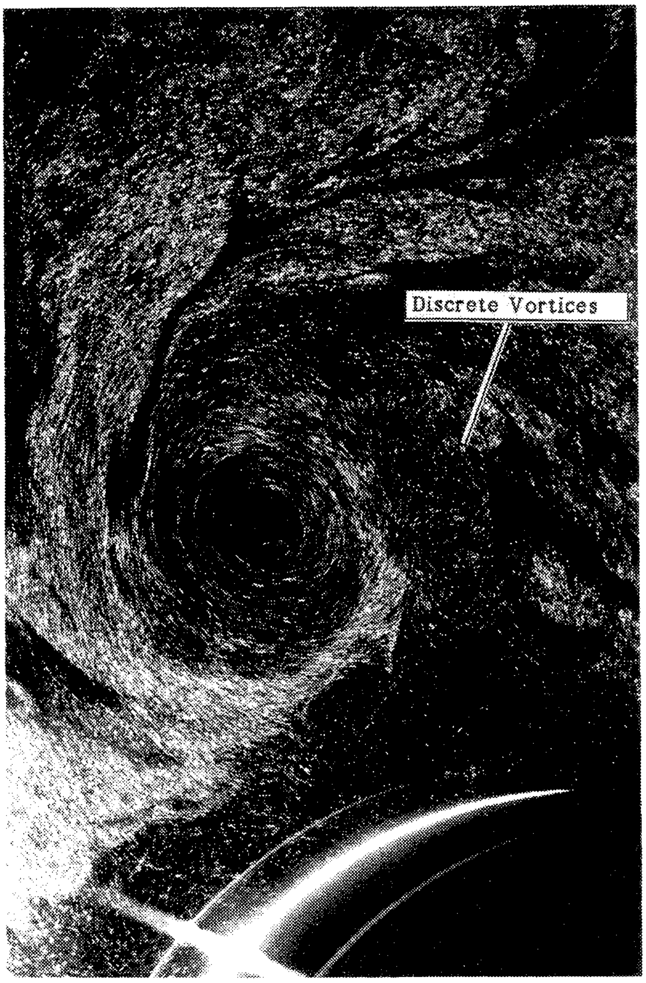

Fig. 2c A typical photograph of the tip vortex downstream of the sail.

inside a SUN 4/260 computer, was used as a frame grabber. Each pixel was assigned an intensity value (gray level) of 0 to 255. The digitized image was enhanced by using different imaging filters (Laplacian, Convolutions, etc.) to improve the signal-to-noise ratio and to augment the clarity of particle traces.

Identifying corresponding traces of particles and extracting displacement information from them required an extensive analysis procedure. Issues of concern were 1) signal identification and noise reduction, 2) matching of the two corresponding traces of the same particle, and 3) edge detection and determination of particle displacement. Noise reduction was handled at two levels, 1) by initial filtering performed on the digitized image, as mentioned earlier, and 2) throughout the process by ignoring incomplete illumination codes. After filtering and enhancement of the image, a pixel-by-pixel and row-by-row search was performed for pixels with gray levels above a preselected threshold, which might represent part of a trace. After examining contiguous pixels of similar gray level, an entire trace was identified and its total size, orientation, and aspect ratio (ratio of major axis over minor axis) were determined. Traces smaller than 10 pixels were considered noise. Next, if the aspect ratio was ≥ 2, it was assumed to be a long trace. With knowledge of the pulse pattern duration (illumination code), the probable location of its corresponding short trace (dot) was predicted. If a dot was found near the estimated location, the particle displacement was calculated. Otherwise, the trace was discarded and the search for another trace continued.

Velocity Measurement

Measurement of particle displacement was calibrated by examining a uniform flow of known velocity. This flow was generated in the tow tank by moving the camera (mounted on the carriage) at a constant velocity past a stationary fluid within a glass fish tank. The tracer particles within the fish tank were illuminated by a longitudinal laser sheet. Velocities recorded were 0.15, 0.3, and 0.6 m/s.

A typical contour map of the energy absorbed by the photographic film is shown in Fig. 3. From similar contour maps, a criterion for mesurement of displacement was established.

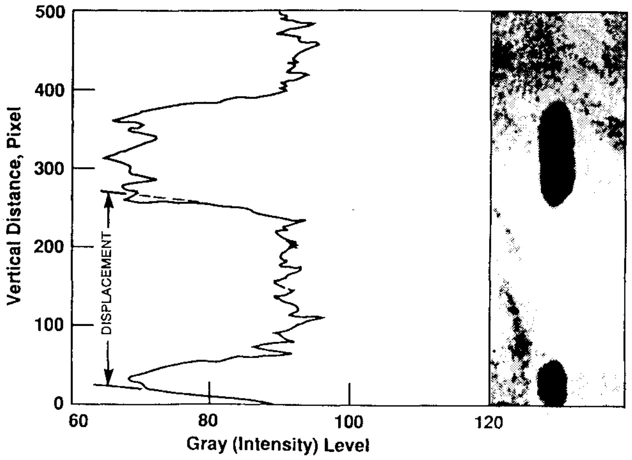

Fig. 3 Contour map of the intensity of particle traces.

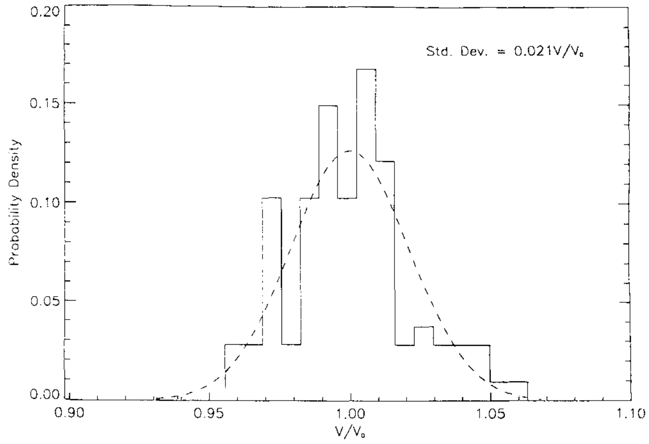

Fig. 4 Velocity histogram of the uniform flow.

According to this criterion, the particle displacement was equal to the distance between the front of the short trace and the front of the long trace. The edge of each trace was identified by the maximum positive slope in the intensity level. Fig. 4 is a probability histogram of the computed displacements. The abscissa is equivalent to the normalized histogram (the bar chart) as well as the calculated probability density function (the broken line). From the results, a standard deviation of $0.021v_0$ was calculated. For a confidence level of 95%, these results suggested that the accuracy in this measurement procedure is in the order of 4.5%.

Since the analysis relied on obtaining one velocity vector per particle and the seed particles were randomly located within the light sheet, the resulting vector map was a conglomerate of randomly positioned velocity vectors. The original velocity vector map was spatially averaged over 2×2-mm^2 cells (real space) to give data on a grid. Linear interpolation was used to estimate the velocity of an unoccupied grid point.

The sources of error in computation of the velocity were as follows:

1) Measurement error varied from 4.5% (from calibration results) to 9% depending on the space between the two traces.

2) Spatial averaging error resulted from forcing the velocity found within a particular averaging cell to be located at the center of the cell (estimated to be in the order of 1%).

3) Interpolation error was the highest contributor to the total error. This error was in the order of 5% for a single interpolation. The uncertainty ranged from 10.5% for an original data point to 15% for a data point resulting from one interpolation.

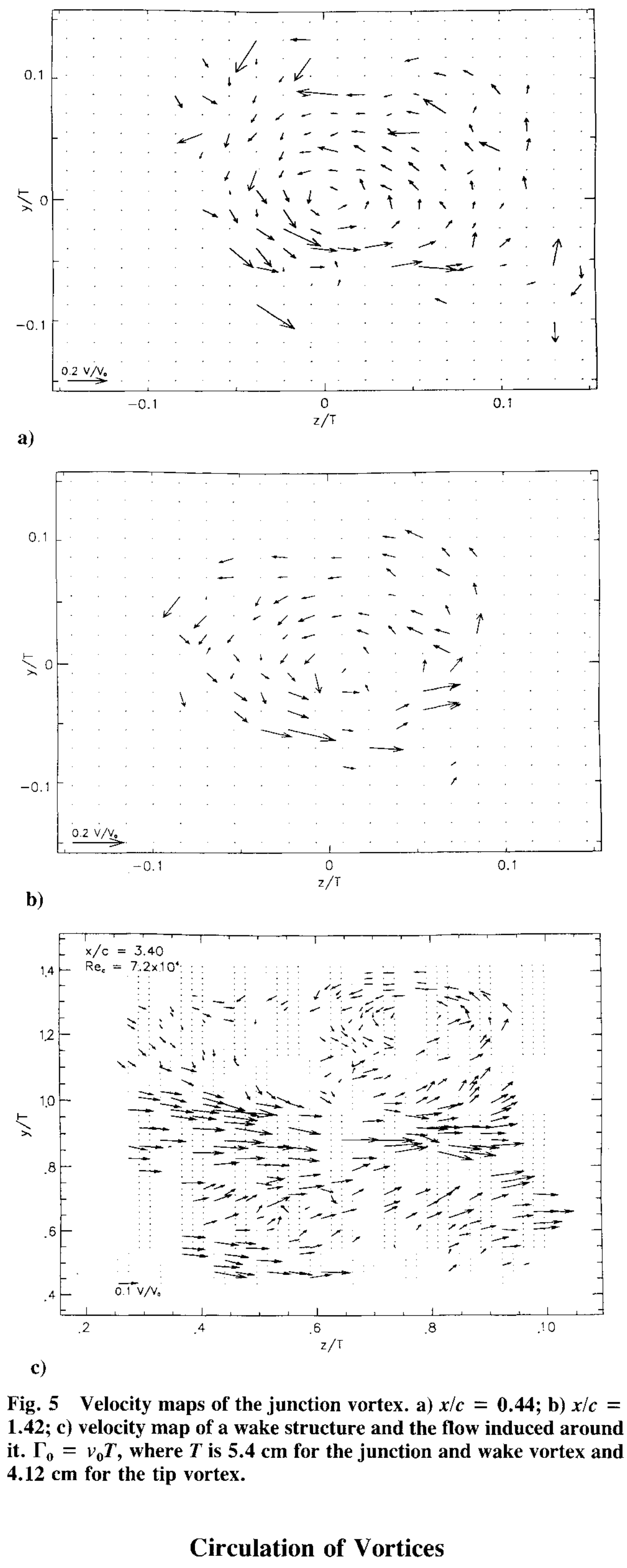

Fig. 5 Velocity maps of the junction vortex. a) $x/c = 0.44$; b) $x/c = 1.42$; c) velocity map of a wake structure and the flow induced around it. $\Gamma_0 = v_0 T$, where T is 5.4 cm for the junction and wake vortex and 4.12 cm for the tip vortex.

Circulation of Vortices

The circulation, Γ, within the area enclosed by a contour C may be found from a line integration defined by the following equation:

$$\Gamma = \oint_c v \cdot \mathrm{d}l \tag{1}$$

where v is the velocity vector, and l is the position vector along C. Implementation of this equation in a rectangular grid required discretization in the following form:

$$\Gamma \cong \sum_i v_{t_i} \cdot \Delta l_i \tag{2}$$

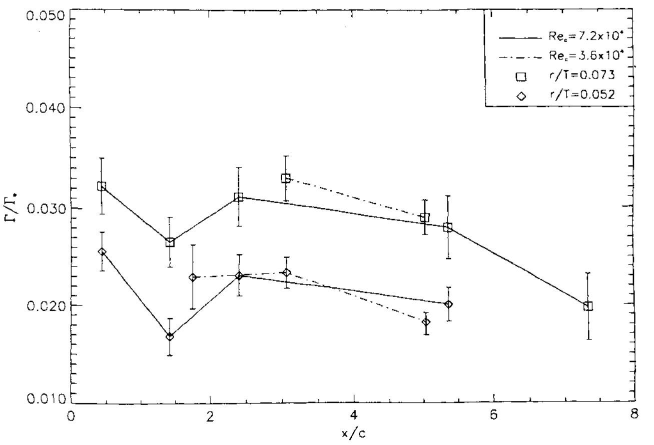

Fig. 6 Dimensionless circulation vs x/c for the junction vortex. $\Gamma_0 = v_0 T$, where T is 5.4 cm.

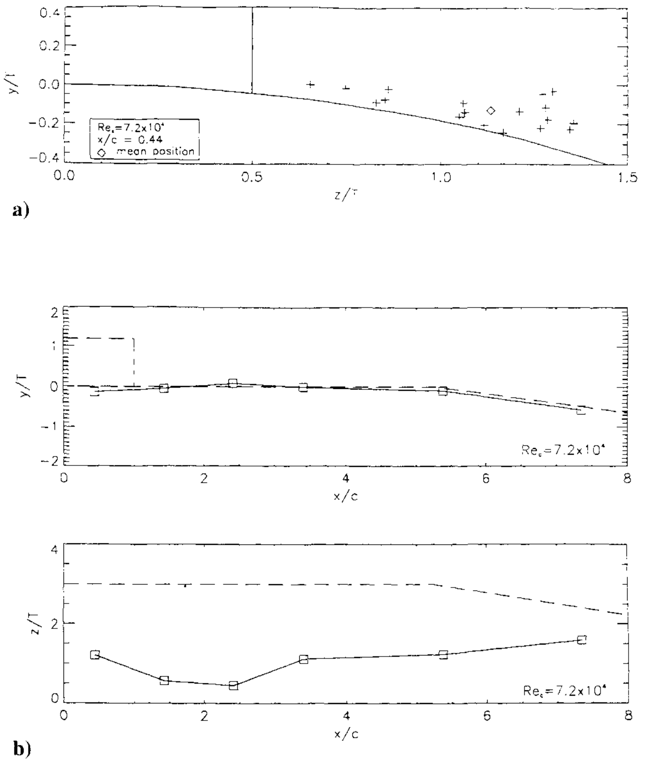

Fig. 7 Plot of a) center location of the junction vortex at $x/c = 0.44$; b) mean location as a function of x/c.

where v_{t_i} is the average tangential velocity of the ith segment of the contour, and Δl_i is the length of that segment.

The circulation and its error were calculated simultaneously. This error was found to be slightly higher than the error in velocity. Depending on the size of a contour and particular velocity data embodied within each contour, the circulation error ranged from 12% to 18%. Three different averaging cell sizes were used in the analysis to investigate the dependence of circulation on cell size. For typical grid spacing varying between 0.25 and 2 mm, the results varied only within ±2%.

Results and Discussion

As mentioned previously, the data presented in this paper consist of the velocity component in a plane normal to the freestream velocity (i.e., lateral velocity). The coordinate system (x,y,z) is marked in Fig. 2a. The origin is at the leading edge of the sail, and x is the streamwise direction. The axial planes studied are $x/c = 0.44$, 1.42, 2.41, 5.37, and 7.34 for the junction vortex and $x/c = 2.89$, 3.89, and 6.89 for the tip vortex, where c is the sail chord length. Several images were recorded at every x/c section. The best sets of data were selected, namely, images with sufficient seed particles for the junction vortex to be visible. The junction vortex at every x/c location was identified by looking at all different x/c locations recorded during the same run and tracking the vortex from one frame to the next. Only clearly identifiable vortices were selected. Conditional sampling of the data involved 1) identifying and analyzing the largest vortical structure with the correct rotational sign in the vicinity of the junction, 2) determining the center of the vortex in each case, 3) combining the instantaneous velocity map of the vortices with the center of all of the vortices overlapping, and 4) spatially averaging and interpolating the resulting velocity map, as described in the preceding section, "Velocity Measurement." The process of superimposing several velocity maps was necessary in the case of the junction vortex because of its size (at most 13 mm in diameter), which limited the number of points per image, and the short residence time close to the surface of the body due to the high longitudinal velocity there. The presence of incomplete illumination codes near the surface from which velocity information could not be extracted supports this argument. Also, the existence of any axial velocity induced within the core of the vortex, as shown by Batchelor,[10] complicates this matter further.

In studying the tip vortex, combining several velocity maps was not necessary, and a single frame yielded a sufficient amount of vectors. The large size of the tip vortex and its location away from the surface helped in this matter. The observed lack of particle traces in the center of the core (Fig.

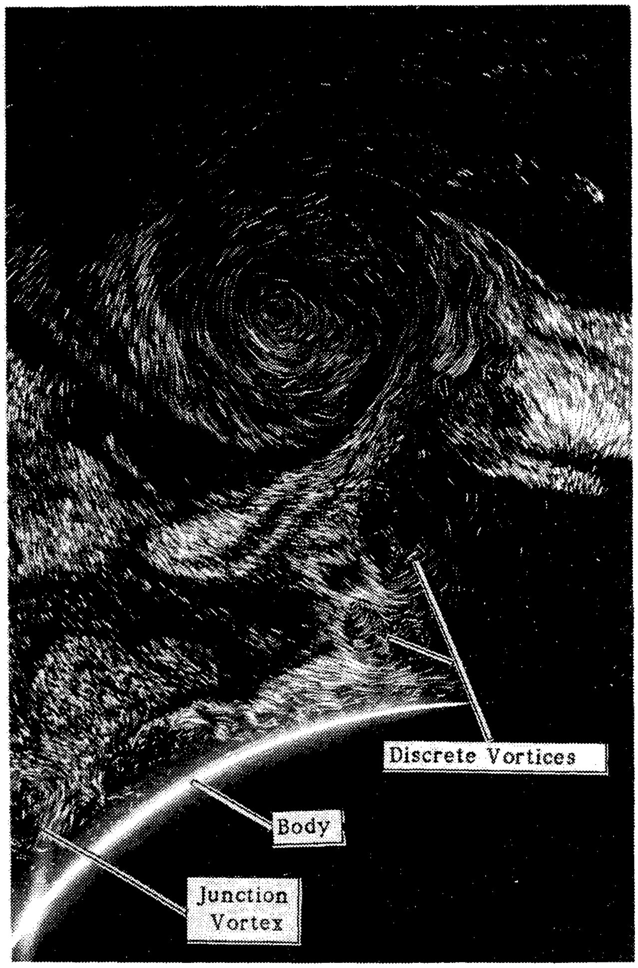

Fig. 8 Qualitative visualization of the tip vortex, $x/c = 2.89$.

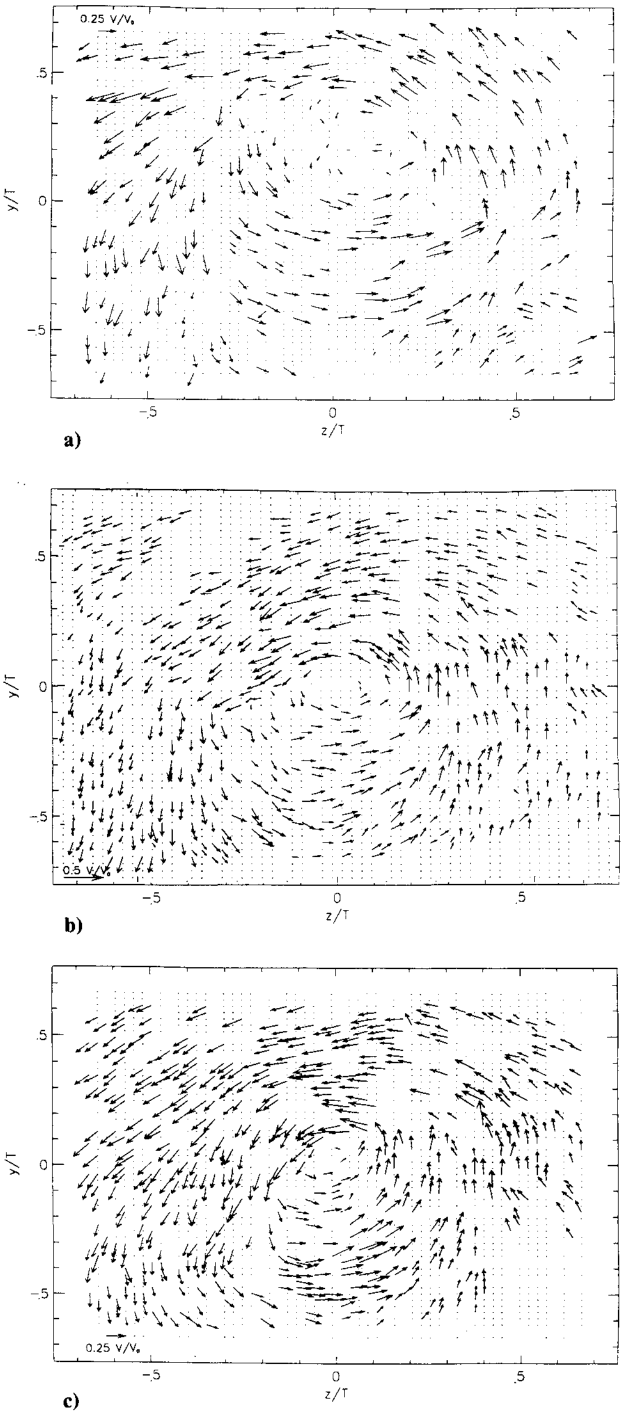

Fig. 9 Velocity maps of the tip vortex. a) x/c = 2.89; b) x/c = 3.89; c) x/c = 6.89.

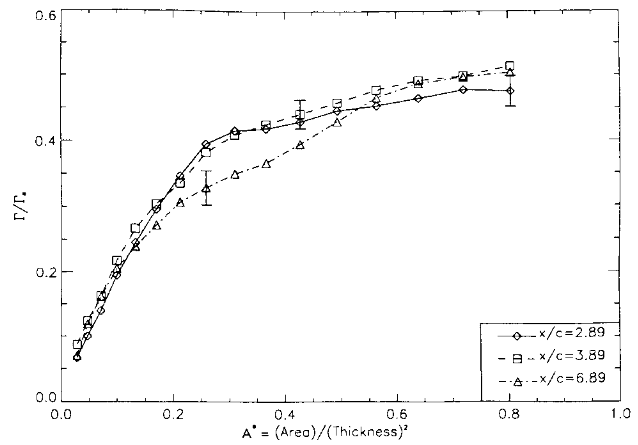

Fig. 10 Circulation profiles of the tip vortex at x/c = 2.89, 3.89, and 6.89. $\Gamma_0 = v_0T$, where T is 4.12 cm.

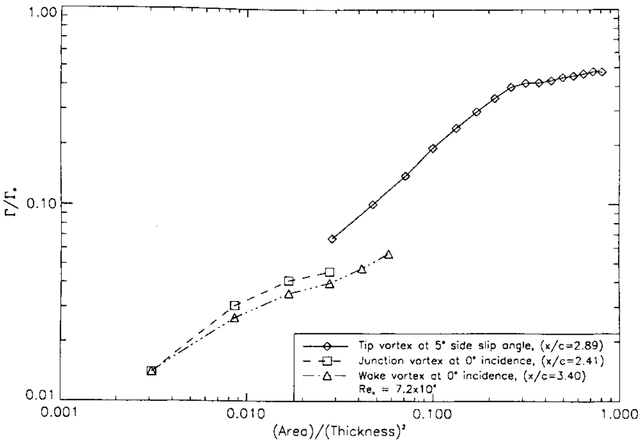

Fig. 11 Comparison among the strengths of the junction vortex, the tip vortex, and a typical wake structure.

2c) was an exception, and it can be attributed to high axial velocities in this region, as discussed earlier. This latter problem was resolved by additional seeding upstream of the light sheet.

Figure 5 contains two velocity maps found by conditional sampling of the junction vortex data. The number of maps sampled at every section decreased in the downstream direction. These numbers ranged between 25 samples at $x/c = 0.44$ to 3 samples at $x/c = 7.34$. Slight detachment of the junction vortex from the surface of the model was observed to take place as x/c increased. This detachment caused an increase in residence time, which yielded a higher number of data points around the vortex and in turn eliminated the need for a high number of samples. As it detached from the surface, the vortex also became circular. As one expects from a vortex located close to a solid body,[8,9] the space between the vortex and the wall is characterized by high velocities. In the present case, v/U_∞ reaches 0.2 at $x/c = 0.44$. This flow is typically modeled as a pair of vortices, and the velocity between is a superposition of the fields induced by both vortices according to Biot-Savart's law.

In general, the geometry and location of the junction vortex was influenced by the lateral freestream flow. Regions of similar lateral freestream flow can be categorized as follows. For $0.44 \leq x/c \leq 1.42$, a relatively uniform flow was directed toward the trailing edge on both sides of the sail, as its thickness decreased. This velocity was relatively small at $x/c = 0.44$ but was measured to be close to $0.25U_\infty$ at $x/c = 0.75$ and persisted for some distance behind the sail. Within the boundary layer, the "primary" junction vortex was clearly visible. The displacement vectors were in most cases very organized and smoothly oriented. A vortex of opposite sign resided adjacent to the primary vortex, usually on the side that was away from the sail. The displacement vectors within this vortex were usually not as large as those within the primary vortex. Other regions of secondary vorticity occasionally appeared around the primary vortex. The presence of some secondary vortex structures is evident in Fig. 5. These structures persisted downstream.

For $1.42 \leq x/c \leq 5.37$ (throughout the parallel middlebody), no significant lateral flow was observed in the region outside the boundary layer and the wake of the sail. The junction vortex initially suffered from lack of coherence at $x/c \approx 1.42$ and became more organized further downstream. However, there were many images in which several corotating vortices in the vicinity and in the same rotational direction as the junction vortex were observed. Within the wake of the sail, very high velocities were observed, at times accompanied by vortices several times larger in size than the junction vortex. The direction of rotation of these vortices varied, and their region of influence frequently included part of the boundary layer near the junction vortex. The influence of these wake structures on the dynamics of the junction vortex may be significant. In fact, the flow in the space between the two junction vortices was strongly dominated by the wake of the sail. A sample characteristic velocity distribution within a small section of the wake is presented in Fig. 5c. Existing computational models[19] compromise this important component of the flow. Measurement of the strength of several wake structures that were located close to the junction show that these vortices are at least as strong as the junction vortex.

For $x/c > 5.37$ a strong axisymmetric flow was produced by contraction of the body. The velocities in this region were on average $0.2U_\infty$. Wavy streamlines suggest the presence of many vortices of various scales embedded within the axisymmetric flow.

Figure 6 is a plot of the dimensionless circulation of junction vortex as a function of x/c. Several values of Γ/Γ_0 for various contour sizes (defined by r, the characteristic radius) are presented at each section. Γ_0 is the product of freestream velocity and sail thickness. The results seem to indicate a reducing trend of the circulation in the downstream direction. The rate of reduction is slower throughout the parallel middlebody than immediately after the sail and in the narrowing afterbody region. These variations in circulation, especially at $x/c = 1.42$, exceed the limits in uncertainty. Several mechanisms can explain the reduction in circulation, such as entrainment of irrotational fluid, diffusion of vorticity, and/or expansion of the vortex. Increase in circulation may be the result of entrainment of corotating vortices or, when the axial flow in the core is faster than the freestream velocity, concentration of the rotational fluid into a smaller area. The results suggest that the circulation scales directly with the freestream velocity and not the square root of velocity, for this range of Reynolds numbers.

Figure 7 is a map of the center location of the junction vortex. Figure 7a demonstrates the actual location of the vortex in individual photographs from which the mean location (also marked) was calculated. The unsteady meandering of the junction vortex is clearly evident. Figure 7b reports the mean location of the junction vortex as a function of x/c. The vortex moved inward to the wake of the sail and then gradually moved outward as x/c increased. This observation is consistent with the reported surface oil visualizations.[3]

The photograph in Fig. 8 is a qualitative visualization of the sail tip vortex. This image was generated by continuous exposure of tracer particles to the laser light. This photograph clearly demonstrates the entrainment of a large number of discrete vortices into the core of the tip vortex. A layer similar to this was described by El-Ramly and Rainbird[13] as the "viscous wake." It appears to be consistent with the roll-up of the "vortex sheet" into the spiraled tip vortex as described by classical models.[10] The junction vortex may also be observed at the left corner adjacent to the surface.

Velocity maps of the tip vortex are presented in Fig. 9. In all of these maps, regions of smaller localized rotation associated with the entrained discrete vortices can be identified. Additionally, the spiral shape of the vortex is clearly visible. The pockets without velocity vectors were created by entrainment of unseeded fluid into the vortex (Fig. 8), as well as by very low velocities. The maximum velocity in these plots usually occurs at $r/T = 0.25$.

In Fig. 10, circulation is plotted against a dimensionless area, A^*, bounded by contours of integration. Careful inspection of this curve, particularly at $x/c = 2.89$, reveals its similarity to the theoretical predictions reported by Hoffman and Joubert,[20] where the circulation follows a r^2 relationship within the central region of the core (i.e., solid body rotation) and a logarithmic profile (i.e., log r) farther out. The region of "solid body rotation" may be identified by the constant slope on the curves. In the downstream direction, this region of solid body rotation becomes smaller. In fact, at $x/c = 6.89$, the radius of this inner region is 50% smaller than that at $x/c = 2.89$.

Finally, the circulation of all junction, tip, and wake vortices (generated behind the sail, such as shown in Fig. 5c) are presented on the same graph, in Fig. 11, for comparison. As is evident from this figure, the strength of the tip vortex is nearly 12 times greater than that of the junction vortex. However, this figure shows that the wake vortex is comparable in strength to the junction vortex.

Conclusions

From the results of the present quantitative visualization experiments, the following conclusions can be drawn. First, PDV offers the ability to visualize a junction vortex even when the vortex is embedded within the boundary layer. Second, the vortex seems to meander, primarily in a direction parallel to the body and less in the direction normal to the surface. Also, the junction vortex detaches from the surface with increasing x/c. Third, the circulation of the junction vortex decreases with increasing x/c. This drop in circulation, for the same contour size, is very gradual within the parallel middle body and becomes steep within the stern region. Observations on the wake of the sail at zero incidence reveal that the strength of a typical wake structure is comparable to that of a junction vortex and that the effect of these wake structures in modeling the junction flow should not be neglected. Additionally, results for two different Reynolds numbers suggest that the circulation is proportional to the freestream velocity, within the range of test conditions.

Profiles of the circulation of the tip vortex as a function of x/c show that its characteristics change only slightly over four chord lengths (from 5.3 to 12.6 spans downstream of the sail). The strength of the tip vortex was observed to increase slightly with x/c, and the maximum circulation of the tip vortex was 12 times greater than that of the junction vortex. Furthermore, the circulation profile for the tip vortex seems to follow the predicted r^2 and log r forms within the inner and outer sections of the core, respectively.

Acknowledgments

This project was supported by ONR (AHR), Naval Sea Systems Command, DARPA Submarine Technology Program, and DTRC IR program. The authors are particularly grateful to Jim Fein from ONR and Gary Jones of DARPA for their continued support and to Peter Congedo for his extensive technical support.

References

[1] Pierce, F. J., and Tree, I. K., "The Mean Flow Structure on the Symmetry Plane of a Turbulent Junction Vortex," *ASME Journal of Fluids Engineering*, Vol. 112, March 1990, pp. 16–22.

[2] Shabaka, I. M. M. A., and Bradshaw, P., "Turbulent Flow Measurements in Idealized Wing/Body Junction," *AIAA Journal*, Vol. 19, No. 2, 1981, pp. 131–132.

[3] Dickinson, S. C., "An Experimental Investigation of Appendage-Flat Plate Junction Flow, Vol. I and Vol. II," DTNSRDC-861-051 and 052, David W. Taylor Naval Ship Research and Development Center, Dec. 1986.

[4] Thwaites, B., *Incompressible Aerodynamics*, Oxford University Press, Oxford, England, UK, 1960.

[5] Schwind, R., "The Three-Dimensional Boundary Layer near a Strut," Gas Turbine Lab. Rep., MIT, Cambridge, MA, 1962.

[6] Baker, C. J., "The Laminar Horseshoe Vortex," *Journal of Fluid Mechanics*, Vol. 95, Pt. 2, 1979, pp. 347–367.

[7]Devenport, W. J., and Simpson, R. L., "Time-Dependent and Time-Averaged Turbulence Structure near the Nose of a Wing-Body Junction," *Journal of Fluid Mechanics*, Vol. 210, 1990, pp. 23–55.

[8]Pauley, W. R., and Eaton, J. K., "Experimental Study of the Development of Longitudinal Vortex Pairs Embedded in a Turbulent Boundary Layer," *AIAA Journal*, Vol. 26, No. 7, 1988, pp. 816–823.

[9]Shabaka, I. M. M. A., Mehta, R. D., and Bradshaw, P., "Longitudinal Vortices Imbedded in Turbulent Boundary Layers. Part 1. Single Vortex," *Journal of Fluid Mechanics*, Vol. 155, 1985, pp. 37–57.

[10]Batchelor, G. K., "Axial Flow in Trailing Line Vortices," *Journal of Fluid Mechanics*, Vol. 20, Pt. 4, 1964, pp. 645–658.

[11]Katz, J., and Bueno Galdo, J., "Effect of Roughness on Rollup of Tip Vortices on a Rectangular Hydrofoil," *Journal of Aircraft*, Vol. 26, No. 3, 1989, pp. 247–253.

[12]McCormick, B. W., Tangler, J. L., and Sherrieb, H. E., "Structure of Trailing Vortices," *Journal of Aircraft*, Vol. 5, No. 3, 1968, pp. 260–267.

[13]El-Ramly, Z., and Rainbird, W. J., "Flow Survey of the Vortex Wake Behind Wings," *Journal of Aircraft*, Vol. 14, No. 11, 1977, pp. 1102–1108.

[14]Adrian, R. J., "Application of Particle Image Velocimetry," *Flow Visualization—1989*, edited by B. Khalighi, M. J. Braun, and C. J. Freitas, Winter Annual Meeting of the ASME, San Francisco, CA, Dec. 10–15, 1989, pp. 23–28.

[15]Gharib, M., and Willert, C., "Particle Tracking: Revisited," *Advances in Fluid Mechanics Measurements*, edited by M. Gad-el-Hak, Springer-Verlag, New York, 1989, pp. 109–199.

[16]Fu, T. C., Bing, R., Katz, J., and Huang, T. T., "Automatic Particle Image Velocimetry Utilizing Laser-Induced Fluorescent Particles," *Proceedings of the 5th International Conference on Numerical Ship Hydrodynamics*, Hiroshima, Japan, Sept. 25–28, 1989, pp. 493–498.

[17]Dong, R., Chu, S., and Katz, J., "Qualitative Visualization of the Flow Structure Within the Volute of a Centrifugal Pump," 1st Joint ASME/JSME Fluids Engineering Conference, Portland, OR, June 1991.

[18]Groves, N. C., Huang, T. T., and Chang, M. S., "Geometric Characteristics of DARPA SUBOFF Models," David Taylor Research Center Report, DTRC/SHD-1298-01, March 1989.

[19]Sung, C. H., and Griffin, M. J., "Improvements in Incompressible Turbulent Horseshoe Vortex Junction Flow Calculations," AIAA 28th Aerospace Sciences Meeting, AIAA Paper 91-0022, Reno, NV, Jan. 7–10, 1991.

[20]Hoffman, E. R., and Joubert, P. N., "Turbulent Line Vortices," *Journal of Fluid Mechanics*, Vol. 16, 1963, pp. 395–411.